

## FEATURES OF THE SUPERCRITICAL TRANSITION IN THE WAKE OF A CIRCULAR CYLINDER\*

Xiong Jun (熊俊)<sup>1,2</sup> Ling Guocan (凌国灿)<sup>2</sup> Zhu Keqin (朱克勤)<sup>1</sup>

<sup>1</sup>(Department of Engineering Mechanics, Tsinghua University, Beijing 100084, China)

<sup>2</sup>(State Key Laboratory of Nonlinear Mechanics, Institute of Mechanics, Chinese Academy of Sciences, Beijing 100080, China)

**ABSTRACT:** The features of the wake behind a uniform circular cylinder at  $Re = 200$ , which is just beyond the critical Reynolds number of 3-D transition, are investigated in detail by direct numerical simulations by solving 3-D incompressible Navier-Stokes equations using mixed spectral-spectral-element method. The high-order splitting algorithm based on the mixed stiffly stable scheme is employed in the time discretization. Due to the nonlinear evolution of the secondary instability of the wake, the spanwise modes with different wavelengths emerge. The spanwise characteristic length determines the transition features and global properties of the wake. The existence of the spanwise phase difference of the primary vortices shedding is confirmed by Fourier analysis of the time series of the spanwise vorticity and attributed to the dominant spanwise mode. The spatial energy distributions of various modes and the velocity profiles in the near wake are obtained. The numerical results indicate that the near wake is in 3-D quasi-periodic laminar state with transitional behaviors at this supercritical Reynolds number.

**KEY WORDS:** cylinder, wake, transition, direct numerical simulation (DNS)

### 1 INTRODUCTION

The extensive studies with both experiments and numerical simulations of the wake behind a circular cylinder at various Reynolds numbers have been carried out for nearly a century. Now it is well-known that the primary instability of the wake leads to the 2-D Kármán vortex street, that is the result of Hopf bifurcation of the steady wake behind the cylinder. And the 3-D transition results from the instability of the 2-D periodic wake to the spanwise disturbances, which is known as the secondary instability.

Two different modes of 3-D vortex shedding in wake transition in the regime  $180 < Re < 260$ , namely, mode A and mode B, were demonstrated by Williamson<sup>[1]</sup>. They involve vortex loops and streamwise vortex pairs. In mode A, the primary vortices deform in a wavy fashion along their length during the shedding process. They result in the local spanwise formation of vortex loops, which become stretched into streamwise vortex pairs.

---

Received 14 October 2001, revised 11 March 2002

\* The project supported by the State Key Fundamental Research Project of "Large Scale Scientific Computation Research" (G199903281)

The spanwise length scale of these vortex loops is around 3 to 4 diameters. When Reynolds number increases, the energy gradually transfers from mode A to mode B. In mode B, finer-scale streamwise vortex pairs are formed. The primary vortex deformation is more spanwise-uniform than in mode A, and the streamwise vortex structure has a markedly smaller spanwise wavelength of around one diameter.

The existence of modes A and B is justified by the 3-D numerical studies of Zhang & Fey et al.<sup>[2]</sup>, Thompson & Hourigan<sup>[3]</sup>, Persillon & Braza<sup>[4]</sup>, Yu<sup>[5]</sup> and Ling & Yu et al.<sup>[6]</sup>, as well as the Floquet stability analysis of Barkley & Henderson<sup>[7]</sup>. Persillon & Braza<sup>[4]</sup> also reported spatial distributions of the mean velocities and the mean square root (RMS) of velocity fluctuations, as well as spectral distributions of the time-domain velocity signals in the regime  $100 < Re < 300$ .

Henderson<sup>[8]</sup> investigated the wake transition in the regime  $100 < Re < 300$  by 3-D direct numerical simulations. In the framework of interactions among mode A, mode B and the primary vortices, he provided an interpretation on how the wake of a cylinder evolves from 2-D to 3-D, and eventually to a state of spatiotemporal chaos. He suggested that three-dimensionality in the wake leads to the irregular states of the flow and fast transition to turbulence at Reynolds numbers just beyond the onset of the secondary instability. A key feature of the transition is the competition between self-excited 3-D instability modes in the mode A wavenumber band.

The studies on the onset features and nonlinear evolution of 3-D instability can contribute to the understanding of how the wake transits into 3-D and to the turbulence as Reynolds number increases. In this respect, however, some important problems still remain open. For instance, when employing spectral expansion in the spanwise direction, the spanwise characteristic length  $L$  and the number of modes  $M$  determine the number and the wavelengths of the possible spanwise modes in the flow. So different values of  $L$  and  $M$  may lead to different flow patterns. The obtained flow may not be identical with the ideal case with infinite spanwise length and infinite modes. However, from the point of view that with finite  $L$  and  $M$ , some specific group of spanwise modes can be picked out of infinite ones, it is possible to isolate the interactions among these typical modes. Thus, studies on how the transition features of the wake change with  $L$  (and  $M$  in the spectral method) are significant. But the work in this respect is lacking. The numerical simulations with different  $L$  have provided quite different results. In previous simulations of the 3-D wake for system size  $L/D = \pi/2$ , Karniadakis & Triatafyllou<sup>[9]</sup> observed a period-doubling bifurcation at  $Re = 300$  and proposed that the wake might follow a period-doubling route to turbulence. In simulations of 3-D wake at  $Re = 265$ , Henderson<sup>[8]</sup> found that the flow state turned from time-periodic mode B to quasi-periodic mixed A-B, then to spatiotemporal chaos when  $L/D$  increases from 0.822 to 3.288, then to 13.152, respectively. And he suggested that the wake follows the Ruelle-Takens-Newhouse (RTN) route to turbulence for sufficiently large  $L$ . However, we are still far from a complete understanding. And one of the purposes of the present work is to provide detailed results about the effect of  $L$  and  $M$  on the supercritical 3-D transition of the wake, which is seldom mentioned in the previous studies. The present investigation of the wake concentrates on a supercritical Reynolds number of 200, which is just beyond the inception of 3-D transition of the cylinder wake and is seldom addressed by previous work. The remainder of this paper will investigate in detail the temporal evolution of various spanwise modes, the phase difference of primary vortices shedding and finally the

features of supercritical transition in the wake.

## 2 MATHEMATICAL MODEL

To numerically investigate the flow past a uniform circular cylinder, a right-handed Cartesian coordinate system is established, in which the positive direction of the  $x$  axis is the direction of incoming flow and the  $z$  axis is the axis of the cylinder. The 3-D Navier-Stokes and continuity equations governing the incompressible viscous flow are taken as follows with all variables normalized by the diameter of the cylinder  $D$  and the uniform stream velocity  $U$

$$\partial \mathbf{V} / \partial t = -\nabla p + \nabla^2 \mathbf{V} / Re + \mathbf{N}(\mathbf{V}) \quad (1)$$

$$\nabla \cdot \mathbf{V} = 0 \quad (2)$$

where the Reynolds number is defined as  $Re = UD/\nu$ , in which  $\nu$  is the kinematic viscosity, and  $\mathbf{N}(\mathbf{V}) = -\mathbf{V} \cdot \nabla \mathbf{V}$  represents the nonlinear convection operator in the Navier-Stokes equations.

## 3 NUMERICAL FORMULATION

Considering the geometric shape of the infinite uniform circular cylinder, mixed spectral-spectral-element method is employed in 3-D numerical simulations of the wake transition of the cylinder, i.e. the Fourier spectral method in the spanwise direction and the spectral element method suggested by Patera<sup>[10]</sup> in the  $x$ - $y$  plane. The spectral element method combines the geometric flexibility of the finite element method with the exponential convergence property of the spectral method. The detailed implementation of spectral element method can be found in Korczak & Patera<sup>[11]</sup> and Karniadakis & Triantafyllou<sup>[9]</sup>.

### 3.1 Spanwise Fourier Spectral Discretization

Velocity  $\mathbf{V}$  and pressure  $p$  are expanded in spanwise direction into the form of Fourier series

$$\mathbf{V}(x, y, z, t) = \sum_{k=-M+1}^M \mathbf{V}_k(x, y, t) e^{i\beta k z} \quad p(x, y, z, t) = \sum_{k=-M+1}^M p_k(x, y, t) e^{i\beta k z} \quad (3)$$

where  $M$  is the number of Fourier modes,  $\beta = 2\pi/L$ , in which  $L$  denotes the spanwise characteristic length, i.e. spanwise periodic length. So the Navier-Stokes and continuity equations are transformed into the forms

$$\partial \mathbf{V}_k / \partial t = -\nabla p_k + (\nabla_{xy}^2 - k^2 \beta^2) \mathbf{V}_k / Re + \mathbf{F}_k[\mathbf{N}(\mathbf{V})] \quad (4)$$

$$\nabla \cdot \mathbf{V}_k = 0 \quad (5)$$

where  $\mathbf{F}_k[\mathbf{N}(\mathbf{V})]$  is the  $k$ th component of the Fourier transform of  $\mathbf{N}(\mathbf{V})$ , which is evaluated by pseudo-spectral method. And the aliasing error is eliminated by truncation.

### 3.2 Time Discretization

The time discretization of Eq.(4) is made using a high-order splitting algorithm based on the mixed stiffly stable scheme suggested by Karniadakis, Israeli & Orszag<sup>[12]</sup>. The

solving procedure is split into three steps

$$\left( \mathbf{V}_k^{n+1/3} - \sum_{q=0}^{J-1} \alpha_q \mathbf{V}_k^{n-q} \right) / \Delta t = \sum_{q=0}^{J-1} \beta_q \mathbf{F}_k [N(\mathbf{V}^{n-q})] \quad (6)$$

$$\left( \mathbf{V}_k^{n+2/3} - \mathbf{V}_k^{n+1/3} \right) / \Delta t = -\nabla p_k^{n+1} \quad (7)$$

$$\left( \gamma_0 \mathbf{V}_k^{n+1} - \mathbf{V}_k^{n+2/3} \right) / \Delta t = (\nabla_{xy}^2 - k^2 \beta^2) \mathbf{V}_k^{n+1} / Re \quad (8)$$

where  $\mathbf{V}^{n+1/3}$  and  $\mathbf{V}^{n+2/3}$  are intermediate values of the velocity variables,  $\alpha_q$  and  $\beta_q$  are implicit/explicit weight coefficients for the stiffly stable scheme of order  $J$ , and  $\gamma_0$  is the weight coefficient of the backwards differentiation scheme. The values of these coefficients for  $J = 3$ , which is employed in this paper, are listed in Table 1.

**Table 1 Values of weight coefficients of the mixed stiffly stable scheme for  $J = 3$**

$\gamma_0$	$\alpha_0$	$\alpha_1$	$\alpha_2$	$\beta_0$	$\beta_1$	$\beta_2$
11/6	3	-3/2	1/3	3	-3	1

The Poisson equation for pressure is

$$\nabla^2 p_k^{n+1} = \nabla \cdot \left( \mathbf{V}_k^{n+1/3} / \Delta t \right) \quad (9)$$

with the consistent high-order boundary condition

$$\partial p_k^{n+1} / \partial n = \mathbf{n} \cdot \left\{ \sum_{q=0}^{J-1} \beta_q \mathbf{F}_k [N(\mathbf{V}^{n-q})] - 1/Re \sum_{q=0}^{J-1} \beta_q \nabla \times (\nabla \times \mathbf{V}_k^{n-q}) \right\} \quad (10)$$

so the  $J$ th-order time accuracy of the splitting scheme is preserved. In Eq.(10)  $\mathbf{n}$  denotes the unit vector normal to the computational domain boundary  $\Gamma$ .

### 3.3 Spatial Discretization in the $x$ - $y$ Plane

Spectral element method is employed to solve the Helmholtz Eqs.(8) and (9), which can be written into the form of a generic modal equation associated with the variable  $u$

$$\begin{cases} \nabla_{xy}^2 u - \lambda u = f & (\lambda \geq 0) & \text{in } \Omega \\ u = g & & \text{on } \Gamma_g \\ \partial u / \partial n = h & & \text{on } \Gamma_h \end{cases} \quad (11)$$

According to the variational principle of the boundary-value problem of the elliptic equations, the modal Eq.(16) is equivalent to

$$\int_{\Omega} (\nabla u \cdot \nabla \delta u + \lambda u \delta u + f \delta u) d\Omega - \int_{\Gamma_2} h \delta u d\Gamma = 0 \quad (12a)$$

$$u|_{\Gamma_g} = g \quad (12b)$$

Assume that the computational domain  $\Omega$  is partitioned into a set of quadrilaterals, each of which is mapped from the  $x$ - $y$  plane into the  $\xi$ - $\eta$  plane by an isoparametric

tensor-product mapping  $\xi = \xi(x, y)$ ,  $\eta = \eta(x, y)$  ( $\xi, \eta \in [-1, 1]$ ). The determinant of the corresponding Jacobian matrix is

$$J = (\partial x / \partial \xi)(\partial y / \partial \eta) - (\partial x / \partial \eta)(\partial y / \partial \xi) \quad (13)$$

Assume that  $x_i$  ( $i = 0, 1, \dots, N$ ) are the Gauss-Lobatto collocation points in the interval  $[-1, 1]$  and  $l_i(x)$  the associated Lagrange interpolating functions of order  $N$ . So  $l_i(\xi)l_j(\eta)$  ( $i, j = 0, 1, \dots, N$ ) are the basis functions in the  $\xi$ - $\eta$  plane. And any function  $u(\xi, \eta)$  (including geometry, velocities and pressure) in the element can be interpolated as

$$u(\xi, \eta) = \sum_i \sum_j u_{ij} l_i(\xi) l_j(\eta) \quad (14)$$

Evaluation of the integral form Eq.(12) gives the elemental equations

$$\sum_{i,j} A_{mnij} u_{ij} = b_{mn} \quad m, n = 0, 1, \dots, N \quad (15)$$

where

$$A_{mnij} = \sum_{k,l} \sum_{p,q} \sum_{o,t} |J_{ot}|^{-1} \tilde{\nabla}_{ijkl} \cdot \tilde{\nabla}_{mnpq} B_{kpo} B_{lqt} + \lambda \sum_{k,l} |J_{kl}| B_{imk} B_{jnl} \quad (16)$$

$$b_{mn} = - \sum_{k,l} \sum_{p,q} |J|_{pq} f_{kl} B_{kmp} B_{lnq} + \int_{\Gamma_2} l_m(\xi) l_n(\eta) (-Y dx + X dy) \quad (17)$$

and

$$\tilde{\nabla}_{ijkl} \equiv \left[ \tilde{\nabla} (l_i(\xi) l_j(\eta)) \right]_{kl} \quad B_{ijk} \equiv \int_{-1}^1 l_i(x) l_j(x) l_k(x) dx \quad (18)$$

$$\mathbf{n} \cdot (X \mathbf{e}_x + Y \mathbf{e}_y) = h \quad (19)$$

in which  $\mathbf{n}$  denotes the unit vector normal to the boundary  $\Gamma_h$ . The global equations can be obtained through the direct stiffness summation.

In the implementation of spectral element method, one can choose different type of Gauss-Lobatto collocation points, such as the Gauss-Lobatto-Chebyshev (GLC) points employed in Korczak & Patera<sup>[11]</sup> and the Gauss-Lobatto-Legendre (GLL) points in Karniadakis & Triantafyllou<sup>[9]</sup>. The former is adopted in this work for its explicit formulations.

#### 4 NUMERICAL RESULTS

Before carrying on 3-D numerical simulations at  $Re = 200$ , tests on 2-D flow at  $Re = 100$  are performed to verify the reliability of the algorithm and the program codes and to assess the effect of the size of the computational domain on the numerical results. Computational domains with different mesh size are used in the tests. The typical meshes are shown in Fig.1. The parameters of the 2-D cases used in the tests are listed in Table 2, where  $XL_1$  and  $XL_2$  are the distances from the axis of the cylinder to the inlet and the outlet boundaries, respectively,  $YL$  is the distance between the upper and lower boundaries,  $NE$  is the number of the elements in the domain,  $NT$  is the number of the nodes on the

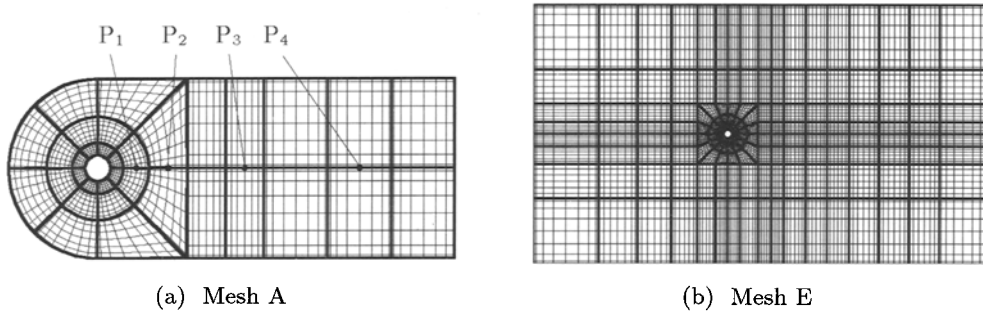


Fig.1 Typical 2-D meshes,  $P_1 \sim P_4$  indicate the positions in the domain of computation where the flow field quantities are recorded in the 3-D simulations

**Table 2 Parameter of the size of the meshes used**

Mesh	$XL_1/D$	$XL_2/D$	$YL/D$	$NE$	$NT$
A	3.5	14	7	34	614
B	6.5	14	13	50	862
C	10.5	30	21	90	1502
D	15	30	21	176	2896
E	22.5	30	30	184	3024

element interfaces and represents the scale of the equations to be solved. The comparison of the obtained Strouhal number  $St = fd/U$  between our simulation tests and the previous experimental and numerical researches<sup>[4,7,13~18]</sup> confirms the reliability of the algorithm and the program codes.

The selected dimensionless spanwise characteristic lengths of the cylinder  $L/D$  and the corresponding numbers of Fourier modes are listed in Table 3. Since mode A, the length scale of which is around 4 diameters, plays an important role in the wake behind a circular cylinder at  $Re = 200$ ,  $L/D$  is chosen as  $4k$ , where  $k$  is a positive integer, to ensure that mode A is included.

**Table 3 Selected cases of spanwise characteristic length and corresponding number of Fourier modes. Also the permitted discrete modes in mode A band and dominant modes, respectively**

Spanwise characteristic length	Number of Fourier modes	Permitted wave length in mode A band	Dominant mode	
			Wave length	Whether in the mode A band
4	16	4	4	yes
8	32	4	4	yes
12	32	4	6	no
		4.8		
24	64	4	24	no
		3.43		

Because of the limitation of available computer resources, the simulations employ mesh A illustrated in Fig.1(a) as the mesh in  $x$ - $y$  plane. The dimension reference length is the radius of the cylinder  $R$ . The time step  $\Delta t = 0.01$ . At  $t = 0$ , the initial disturbance along  $z$  direction, which is in a triangular-shaped distribution with a maximum amplitude of 0.1, is added to the streamwise velocity  $u$  in the domain  $x < 0$ . When  $t > 0$ , the artificial

disturbance is removed in computation. The numerical results of 3-D evolution of the wake behind a circular cylinder at  $Re = 200$  are presented in the following paragraphs.

#### 4.1 The Spanwise Modes of the Near Wake Flow

For  $Re = 200$ , the wavelength range of instability mode A band is  $(3.25D, 5.13D)$  according to the Floquet stability analysis in Barkley & Henderson<sup>[7]</sup>. And the discrete wavelengths of the modes in the mode A band, which are determined by  $L$  and  $M$ , are listed in Table 3.

First let us examine the temporal development and interactions of different spanwise modes with the time series of their kinetic energy

$$E_k(t; x, y) = (u_k^2 + v_k^2 + w_k^2) / 2 \quad k = 0, 1, 2, \dots, M/2 - 1 \quad t > 0 \quad (20)$$

at specific  $(x, y)$  points in the flow field. The  $E_k(t)$  curves of typical modes at the point  $P_1$  for  $L/D = 12$  are shown in Fig.2. Note that the ranges of the vertical coordinate in the figures vary with different modes.

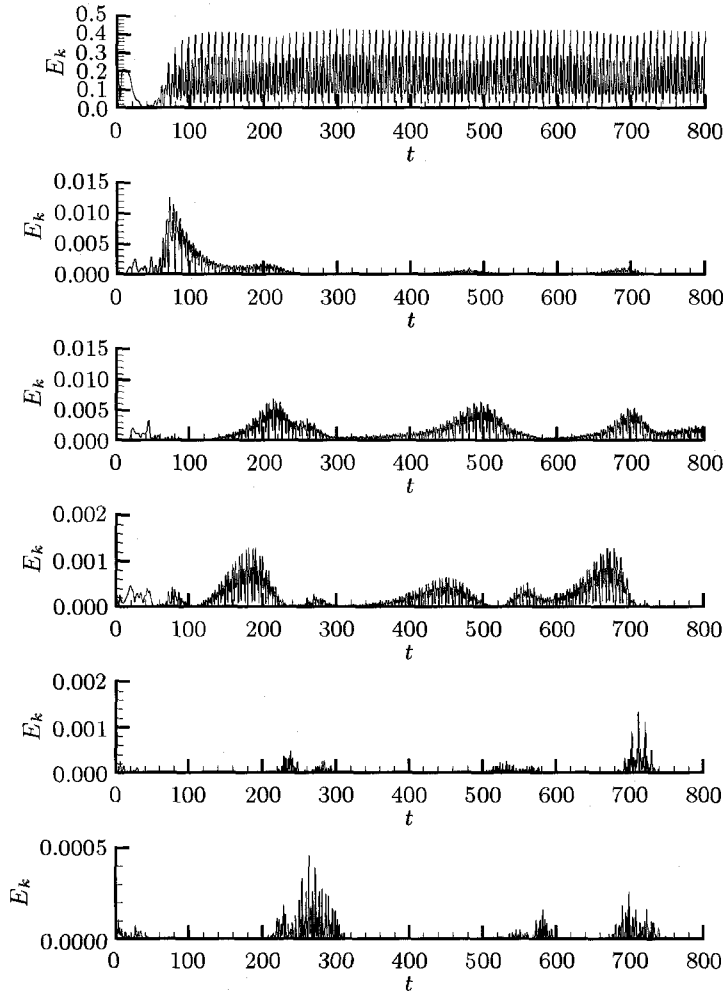


Fig.2 Time series of kinetic energy of the spanwise modes,  $k = 0, 1, 2, 3, 10$  and  $13$  (from the top to down), at point  $P_1$  for  $L/D = 12$

The evolution of Fourier modes illustrated in Fig.2 differs distinctly from the cases described by the linear stability theory, which concerns with disturbance of small amplitude<sup>[7,8]</sup>. According to the linear stability theory, the linear unstable modes are induced directly by small disturbance at an early stage of the evolving process of the flow; while other linear stable modes emerge through their nonlinear interactions with the developed unstable modes. However, in the present work we found that the peaks of marked amplitude appear in the early stage of the  $E_k(t)$  curves at more modes, not only those linear unstable modes in mode A band, such as the mode  $k = 1 (\lambda = 12D)$  for  $L/D = 12$  (in Fig.2). It indicates that some modes being stable predicted by linear analysis, as well as those linear unstable ones, are directly induced, and the time needed for all the modes to tend to some kind of dynamical equilibrium is shortened a great deal, which is one of the motivations of introducing initial disturbance with a finite amplitude.

Although all the spanwise modes involved in the present computation emerge, the amplitudes of their kinetic energy differ a great deal. The dominant spanwise mode can be determined by the mean energy averaging in its equilibrium interval at specific points in the flow field, which is shown in Fig.3. The equilibrium interval is determined by the time series of velocity at the chosen points. For example, see the time series of velocity components  $u$

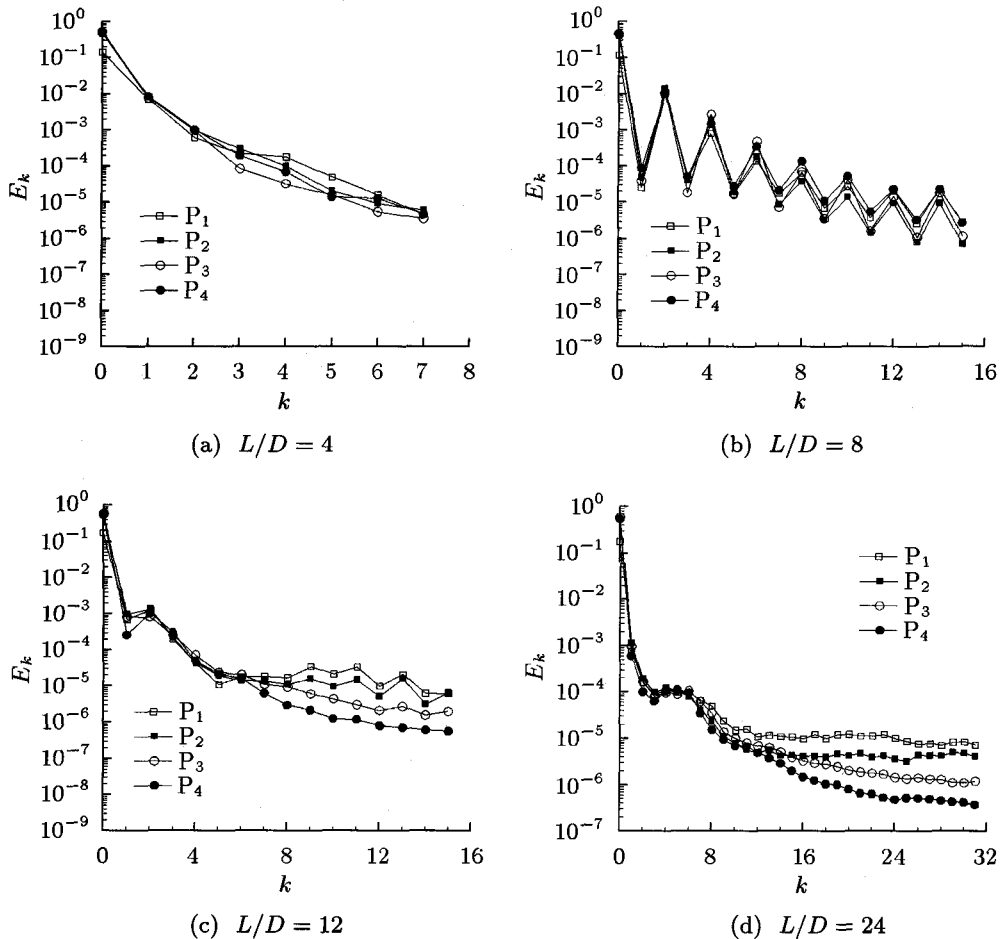


Fig.3 Mean kinetic energy in the equilibrium interval at four points shown in Fig.1



and  $v$  at point  $P_1(z = 0)$  for  $L/D = 24$ . For various  $L/D$ , the velocity signal becomes quasi-periodic when  $t > 100$  and the effect of initial disturbance vanishes, so the temporal interval  $[100, 500]$  is regarded as the equilibrium interval, in which the mean energy is evaluated. Note that although the most part of kinetic energy is held in mode  $k = 0$ , it is excluded in our discussion on spanwise modes because it corresponds the energy of a uniform flow and does not represent patterns. The obtained dominant modes for various  $L/D$  are listed in Table 3 for convenience of comparison. It is worth noting that for  $L/D = 12$ , mode  $k = 3$  is the sole linear unstable mode, but its mean kinetic energy is less than that for mode  $k = 2$ . So in this situation the dominant mode is not mode A but the mode  $\lambda = 6D$ . No similar case where the linear stable mode becomes the dominant mode in the wake, overwhelming mode A, was previously reported.

The contours of streamwise vorticity shown in Fig.4 confirm that the dominant modes in the flow field for  $L/D = 4$  and 12 are modes  $\lambda = 4D$  and  $6D$ , respectively. These results confirm the above arguments. Our results show that the spanwise characteristic length selected in the computations determines the dominant mode in the flow field. For some  $L/D$ , for example,  $L/D = 12$ , the specific mode predicted to be stable by the linear stability theory can be excited and become a dominant mode. Consequently  $L/D$  has a great effect on the global properties of the flow field. Comparison of the energy distributions among the spanwise modes for different  $L/D$  can lead to the conclusion that in the flow at  $Re = 200$  investigated in the present work, from upstream to downstream in the wake, the energy distribution at small wave number (long wave) modes is in the same level for different  $L/D$ . While the energy of large wave number (short wave) modes for larger  $L/D$ , i.e. 12 and 24, decays much faster downstream than that for smaller  $L/D$ , i.e. 4 and 8. By the way, the energy distribution for  $L/D = 8$  remarkably differs from the other cases by a curve in sawtooth waveform, the origin of which remains to be explained by research in future.

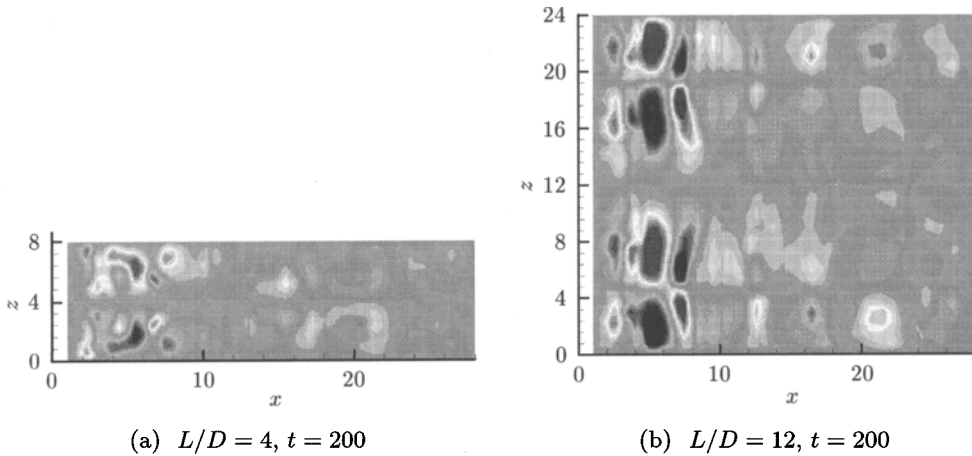


Fig.4 Contours of streamwise vorticity at  $y = 0$

#### 4.2 Average Velocity Profiles

The distributions of time mean values of streamwise velocity  $u$  and transverse velocity  $v$ , denoted as  $U_m$  and  $V_m$ , at the rear axis of the cylinder ( $y = 0$ ) for  $L/D = 4, 8$  and 12 are calculated. The interval for time averaging is chosen as  $[100, 500]$ , too. For the purpose of studying the global features of the flow, the time mean values are also averaged in the

spanwise direction. And it is the same for the RMS of the velocity fluctuation. The results are illustrated in (a), (b) and (c) of Fig.5. The spatial distribution of  $U_m$  is almost the same for different  $L/D$ . When  $x$  increases, its value decreases from zero to negative and then increases to positive, which implies the existence of recirculation region behind the cylinder. And the point of vanishing  $U_m$  from negative to positive determines the reattachment length. In this work it is found that  $x/D = 1.54, 1.56$  and  $1.33$  for  $L/D = 4, 8$  and  $12$ , respectively. It is given by Persillon & Braza<sup>[4]</sup> that  $x/D = 1.28$  at  $Re = 200$ , where the spanwise length of computational domain is  $2.25D$  and  $3.72D$ . As for the spatial distribution of  $V_m$ , the curve for  $L/D = 4$  is close to that of Persillon & Braza<sup>[4]</sup>. While the amplitudes for  $L/D = 8$  and  $12$  are evidently smaller, due to the increase of irregularity of  $v$  with the increase of  $L/D$ . The comparison between the mean velocity profiles at several sections ( $x = 7.0, 13.0$  and  $23.0$ ) for  $L/D = 4$  and  $12$  shown in Figs.6, indicates that the irregularity of  $u$  and  $v$  along the transverse direction increases with the increase of  $L/D$  and decays with the development of the flow downstream.

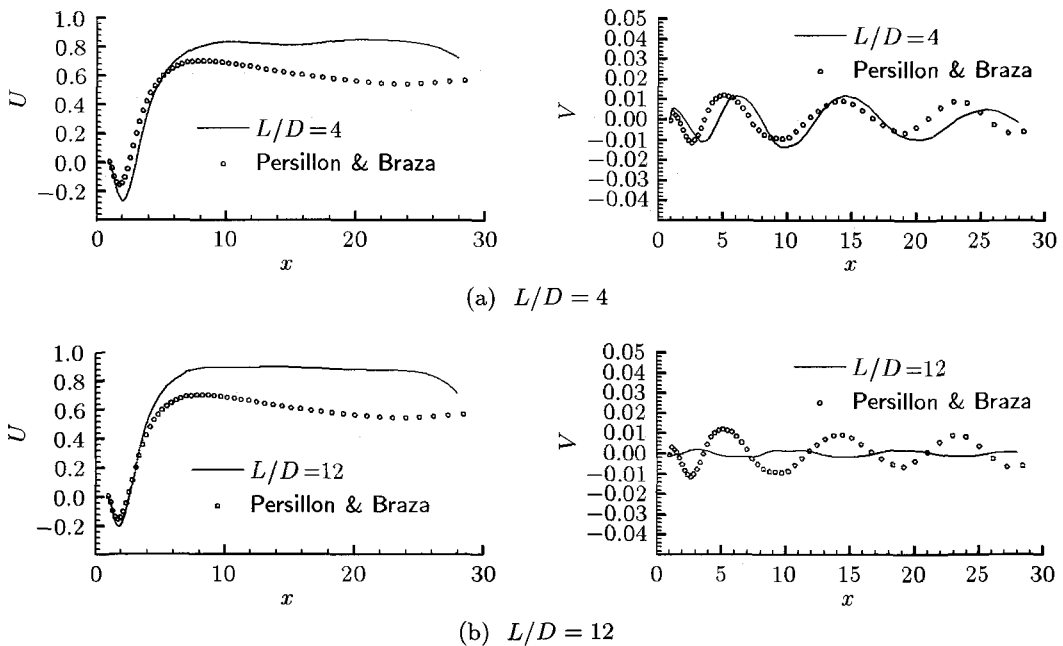


Fig.5 Profiles of streamwise and transverse mean velocity at  $y = 0$ . The circles in (a) and (b), which are identical results, are extracted from Fig.29 and Fig.30 in Persillon & Braza<sup>[6]</sup>, where  $L/D = 2.25$  and  $3.72$

The profiles of streamwise velocity fluctuation RMS  $u'_{\text{rms}}/U$  at sections  $x = 7, 13$  and  $23$  for  $L/D = 12$  are illustrated in Fig.7(b). The cases for  $L/D = 4$  and  $8$  are almost the same. A key feature of these profiles is that they all show two symmetrical peaks no matter in the near wake or in the little far wake, usually associated with the two rows of laminar vortices traveling downstream. Comparing the profiles of  $u'_{\text{rms}}/U$  at three sections shows that the peak value decreases downstream, which results from the energy damping of primary vortices caused by viscous dissipation. But on the rear axis of the cylinder ( $y = 0$ ), the value of  $u'_{\text{rms}}/U$  at  $x = 23$  is slightly larger than that at  $x = 7$  and  $13$ , which is more clearly shown in Fig.7(a). In comparison with the measured RMS profile of the

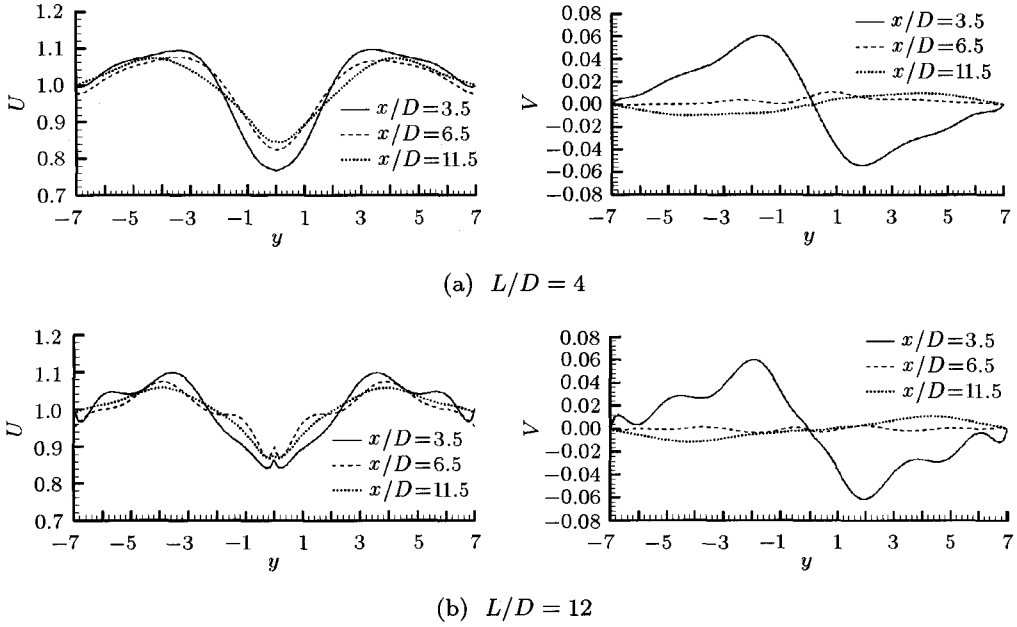
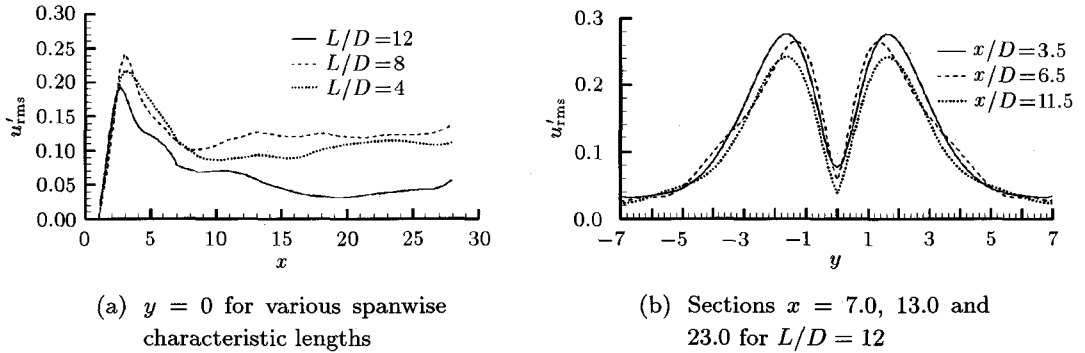
Fig.6 Profiles of mean velocities at sections  $x = 7.0, 13.0$  and  $23.0$ 

Fig.7 Profiles of streamwise velocity fluctuation RMS

streamwise velocity fluctuation in the laminar regime ( $Re = 152$ ) by Williamson<sup>[1]</sup>, which shows two side peaks, we suggest that the near wake at  $Re = 200$  is still laminar.

#### 4.3 Phase Difference of the Primary Vortices Shedding

Fourier analysis of the spanwise vorticity time series at several points in the flow field is carried out to quantitatively study the phase difference of the primary vortices shedding, the origin of which is also explained. Our choice of employing Fourier analysis and putting aside the popular method of isosurfaces of vorticity or pressure is based on the consideration that since the wake of the cylinder has turned into 3-D, the deformation of vorticity and pressure isosurfaces may result from the shedding difference of both phase and intensity. The isosurface itself can not exactly tell the effect of one factor from the other. But Fourier analysis can extract the phase difference from the time series and eliminate the effect of the intensity difference of the spanwise vortices.

The comparison between the phases of the signals of different frequencies makes no sense. As for two signals of the same frequency  $s_1 = \cos(2\pi ft + \theta_{01})$  and  $s_2 = \cos(2\pi ft +$

$\theta_{02}$ ), the phase difference between them is constantly  $\theta_{02} - \theta_{01}$ . A periodic signal  $s(t)$  composed of multiple components of different frequencies can be written into the form  $s(t) = \sum_{k=-\infty}^{\infty} c_k e^{ik\pi t/T}$ , where  $c_k$  denotes the Fourier coefficients. The wave form corresponding the frequency component  $f_k = k/2T$  of signal  $s(t)$  is  $2|c_k| \cos(2\pi f_k t + \arg c_k)$ . So its initial phase is

$$\theta_0(f_k) = \arg c_k = \arctan [\text{Im}(c_k)/\text{Re}(c_k)] \quad (21)$$

Therefore, the initial phase  $\theta(f; x, y, z)$  of any frequency component  $f$  of the spanwise vorticity signal  $\omega_z(t; x, y, z)$  can be evaluated by Eq.(21). Since the most part of the spanwise vortex energy is concentrated in the shedding frequency  $f_s$  of primary vortices, it is taken for granted that the phase difference of  $f_s$  determines that of the spanwise vortices. Shown in Fig.8 are the phase differences  $\theta(z) - \theta_0$  of  $f_s$  in the time series  $\omega_z(t; z)$ , relative to  $\omega_z(t; z_0)$ , which is the spanwise vorticity at  $z = 0$ , at four  $(x, y)$  points marked in Fig.1 for  $L/D = 4$  and 12.

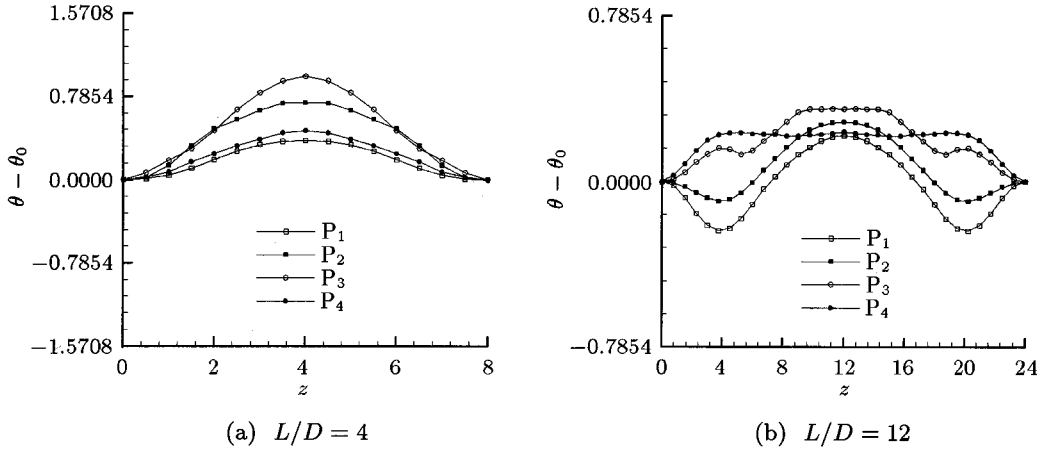


Fig.8 Phase difference of frequency component  $f_s$  of  $\omega_z(t; z)$  relative to  $\omega_z(t; z_0)$

From the phase difference curves of spanwise vortices in the near wake we can investigate the phase difference of the Kármán vortices shedding. In the near wake where the spanwise vortices form (for example, at points  $P_1$  and  $P_2$ ), the wavelength of the phase difference curves is  $4D$  for  $L/D = 4$ , and the phase at the ends of the cylinder takes the minimum and in the middle the maximum; while for  $L/D = 12$ , the wavelength of the curves is  $6D$ , and the phase in the vicinity of  $z = 4$  and  $20$  takes the minimum and in the middle the maximum. During the shedding process the maximum phase difference along the spanwise direction is around  $\pi/2$  for  $L/D = 4$  and around  $\pi/4$  for  $L/D = 12$ . Conjugated with the isosurfaces of streamwise vorticity in Fig.4, the phase difference of the Kármán vortices shedding is suggested to be the result of the development of spanwise modes, and consequently to be determined by the dominant mode in the flow field.

## 5 CONCLUSIONS

Based on the results of the direct numerical simulations we can draw some conclusions on the nonlinear features of the supercritical transition in the wake of a circular cylinder at  $Re = 200$  as below:

- (1) In the supercritical 3-D transition, the nonlinear evolution of 3-D instability causes the coexistence and interactions of the spanwise modes with different wavelengths. One of the most remarkable effects of nonlinear behaviors is the intermittent property of the modes with large wave number during the temporal development.
- (2) The spanwise characteristic length has a great effect on the global properties of the flow field. In the numerical simulations with chosen  $L/D$ , new dominant spanwise modes other than mode A are found, which were not reported by previous work. For some  $L/D$ , the specific mode predicted to be stable by the linear stability theory could become dominant mode in addition to the linear unstable mode. These new dominant modes can result in new features of the transition and the flow field. As for the energy distribution between different spanwise modes at  $Re = 200$ , the increase of the spanwise characteristic length can result in the increase of the portion of mode  $k = 0$  in the total kinetic energy, the damping rate of large wave number modes downstream, and the irregularity of spatial distribution of velocity.
- (3) The primary vortices shedding is 3-D. There are differences in phase along the span. The maximum of the phase difference is relatively small, which is around  $\pi/2$  for  $L/D = 4$  and around  $\pi/4$  for  $L/D = 12$ . And the spanwise wavelength of the phase difference is largely determined by the dominant mode of the flow. It is speculated that the phase difference is produced by the spanwise mode structure.
- (4) The time series of the velocity, vorticity and kinetic energy and the bilobate structure of the RMS profiles of the velocity fluctuation are provided. The results indicate that the flow in the computational domain of this work is essentially in a three-dimensional quasi-periodic transitional laminar state. The flow field at supercritical Reynolds number has shown to be irregular in the span and transverse direction. The irregular state will evolve into the spatiotemporal chaos and even turbulence at higher Reynolds numbers. While at the current Reynolds number of 200, it is suppressed by the viscosity and decayed downstream.

**Acknowledgements** This work is completed in State Key Laboratory of Nonlinear Mechanics, Institute of Mechanics, Chinese Academy of Sciences. The authors are also grateful to LSSC, Institute of Computational Mathematics, Chinese Academy of Sciences for offering the computational circumstances of PC clusters.

## REFERENCES

- 1 Williamson CHK. The natural and forced formation of spot-like dislocations in the transition of a wake. *J Fluid Mech*, 1992, 243: 393~441
- 2 Zhang HQ, Fey U, Noack BR, et al. On the transition of the cylinder wake. *Phys Fluids*, 1995, 7(4): 779~794
- 3 Thompson M, Hourigan K, Sheridan J. Three-dimensional instabilities in the wake of a circular cylinder. *Exp Therm Fluid Sci*, 1996, 12(2): 190~196
- 4 Persillon H, Braza M. Physical analysis of the transition to turbulence in the wake of a circular cylinder by three-dimensional Navier-Stokes simulation. *J Fluid Mech*, 1998, 365: 23~88
- 5 Yu CW. On the features of the three-dimensional transition in the wake of a circular cylinder. [PhD Thesis]. Beijing: Institute of Mechanics, CAS, 1998 (in Chinese)
- 6 Ling GC, Yu CW, Xiong ZM. The nonlinear features of the wake transition behind a circular cylinder. In: Lian QX & Kiga M eds. Proceeding of the Third China-Japan Workshop on

- Turbulent Flow, Beijing, 1998-10-03~11-04, Beijing: Beijing Univ of Aero & Astro Press, 1998
- 7 Barkley D, Henderson RD. Three-dimensional Floquet stability analysis of the wake of a circular cylinder. *J Fluid Mech*, 1996, 322: 215~241
  - 8 Henderson RD. Nonlinear dynamics and pattern formation in turbulent wake transition. *J Fluid Mech*, 1997, 352: 65~112
  - 9 Karniadakis GE, Triantafyllou GS. Three-dimensional dynamics and transition to turbulence in the wake of bluff objects. *J Fluid Mech*, 1992, 238: 1~30
  - 10 Patera AT. A spectral element method for fluid dynamics: Laminar flow in a channel expansion. *J Comput Phys*, 1984, 54(3): 468~488
  - 11 Korczak KZ, Patera AT. An isoparametric spectral element method for solution of the Navier-Stokes equations in complex geometry. *J Comput Phys*, 1986, 62(2): 361~382
  - 12 Karniadakis GE, Israeli M, Orszag SA. High-order splitting methods for incompressible Navier-Stokes equations. *J Comput Phys*, 1991, 97(2): 414~443
  - 13 Roshko A. On the development of turbulent wakes from vortex streets. NACA Rep. 1191, 1954
  - 14 Williamson CHK. The existence of two stages in the transition to three dimensionality of a cylinder wake. *Phys Fluids*, 1988, 31(11): 3165~3167
  - 15 Konig M. The fine structure in the Strouhal-Reynolds number relationship of the laminar wake of a circular cylinder. *Phys Fluids*, 1990, 2(9): 1607~1614
  - 16 Hammache M, Gharib M. An experimental study of the parallel and oblique vortex shedding from circular cylinders. *J Fluid Mech*, 1991, 232: 567~590
  - 17 Norberg C. An experimental investigation of the flow around a circular cylinder: influence of aspect ratio. *J Fluid Mech*, 1994, 258: 287~316
  - 18 Henderson RD. Details of the drag curve near the onset of vortex shedding. *Phys Fluids*, 1995, 7(9): 2102~2121